ACS APPLIED MATERIALS & INTERFACES

Research Article

www.acsami.org

Modification of Mott Phase Transition Characteristics in VO_2@TiO_2 Core/Shell Nanostructures by Misfit-Strained Heteroepitaxy

Yamei Li,[†] Shidong Ji,[†] Yanfeng Gao,[†,‡] Hongjie Luo,[†,‡] and Ping Jin*[,†]

[†]State Key Laboratory of High Performance Ceramics and Superfine Microstructure, Shanghai Institute of Ceramics, Chinese Academy of Sciences, Dingxi 1295, Changning, Shanghai, 200050, China

[‡]School of Materials Science and Engineering, Shanghai University, Shangda Rd. 99, Baoshan, Shanghai 200444, China

Supporting Information

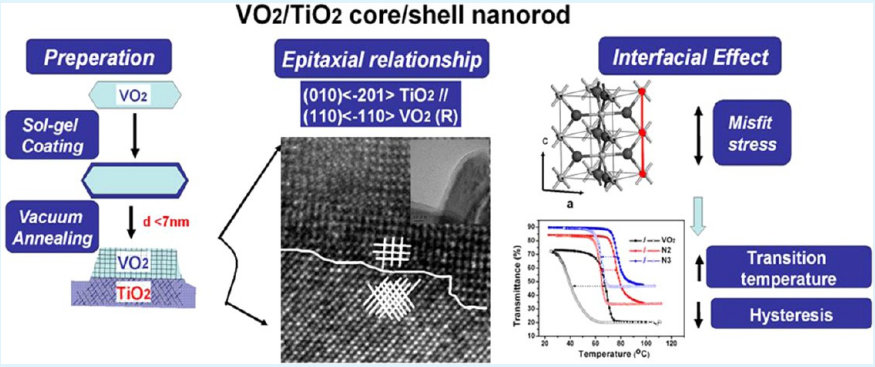

ABSTRACT: Vanadium dioxide (VO_2) is a key material for thermochromic smart windows that can respond to environmental temperature and modulate near-infrared irradiation by changing from a transparent state at low temperature to a more reflective state at high temperature, while maintaining visible transmittance. Here, we demonstrate for the first time that the Mott phase transition characteristics in VO_2 nanoparticles can be remarkably modified by misfit strains occurring at the epitaxial interface between VO_2 and the anatase TiO_2 of VO_2/TiO_2 core−shell particles. The heteroepitaxial growth of the as-synthesized particles followed an unprecedented orientation relationship, and an epitaxial growth mechanism is proposed to explain this behavior. A relatively small theoretical coherent misfit (3−11%) and a moderate heating rate (20 °C·min^{-1}) in the preparation of the core−shell structure were critically important from the thermodynamic and kinetic perspectives, respectively. The misfit-induced interfacial strain along the uniaxial c_R axis increased the transition temperatures, especially on the cooling portion of the heating−cooling cycle, leading to a notably reduced transition hysteresis loop width (from 23.5 to 12.0 °C). Moreover, the optical band gap was also engineered by the interfacial effect. Such a reduced hysteresis showed a benefit for enhancing a rapid response for energy saving thermochromic smart windows.

KEYWORDS: *vanadium dioxide, titanium dioxide, interfacial heteroepitaxy, core−shell, thermochromism, smart window*

1. INTRODUCTION

Strain is critically important in tuning the electronic and/or optical properties of nanosized colloids. Since the adventure of core/shell nanotechnology, the ability of using lattice-mismatched strains to tailor the band energy and carrier transport behaviors in semiconductor colloids has been confirmed. Using the interfacial interactions of a core/shell structure to tune the optical,[1] electrical,[2] or magnetic[3] properties of the core materials has been widely reported. The effect of the internal stress state on the permittivity response of $BaTiO_3$ can be induced by coupling or by the confinement effect at the interface.[2] Recently, a novel strategy to control the light-emitting property of CdSe @CdTe core/shell semiconducting nanoparticles or nanodots[1,4,5] was developed by controlling the interfacial stress, which opened the era of "energy band engineering" or "wave function engineering". In these reports, the thermodynamics of core/shell heteroepitaxy was conventionally held to follow the Stranski-Krastanov model with a large misfit strain energy and the occurrence was only limited to two crystals of the same symmetry. A shell of a few monolayers in thickness can act as a passivation layer and provides a specified potential well to achieve carrier separation and/or manipulation, thus controlling the light emitting efficiency and lifetime. Exploring the interfacial strain effect on functions in other nanosized core/shell heterosystems is of great value from the scientific perspective.

As a typical phase transition compound, the Mott-type semiconductor vanadium dioxide (VO_2) undergoes a fully reversible metal-to-semiconductor phase transition (MST) at

Received: April 9, 2013
Accepted: June 13, 2013
Published: June 18, 2013

   dx.doi.org/10.1021/am401297g | ACS Appl. Mater. Interfaces 2013, 5, 6603−6614

~68 °C (in a bulk crystal). This thermally driven phase transition concurs with a crystallographic transition from a low-temperature monoclinic (M1 phase, space group $P2_1/c$) to a high-temperature tetragonal rutile (R phase, space group $P4_2/mnm$) structure and is accompanied by a rough variation in optical, electrical, and magnetic properties.[6] In particular, the semiconducting M1 phase is nearly transparent in infrared light, whereas the metallic R phase is highly reflective with nearly maintained high luminous transmittances, which is mostly promising for applications in energy-saving smart windows. VO_2 thermochromic coatings/films can be produced using gas phase reactions (e.g., sputtering[7] or chemical vapor deposition[8,9]) or polymer-assisted solution deposition,[10−12] and more recently, VO_2 nanopowder-based flexible foils have been developed by our group using nanopowder dispersions[13,14] and exhibited excellent solar energy modulation efficiency.

The familiar and fundamental factor for inducing Mott phase transitions in correlated VO_2 is heat; some unusual external stimuli, such as light,[15] electric field,[16] stress,[17,18] and/or their combinations, have also been confirmed to have special effects. Currently, the strain effect has been widely studied in VO_2 thin films. Intentionally applying strain to VO_2 particles can remarkably change the relative thermodynamic stability of the M1 and R phases, thus modifying the transition temperature and other opto-electronic properties. Cao et al.[19] demonstrated a novel method for controlling the periodic insulating and metallic phase domains along the VO_2 nanobeams ($//c_R$) by tuning the strain in the VO_2 particle, which lowered the MIT temperature to room temperature. A uniaxial stress parallel to c_R can also be typically formed by substrate mismatch, adhesion,[20] bending,[17] or mechanical manipulation[21] to explore applications in actuators or sensors. In VO_2-based optoelectronic devices,[22] heteroepitaxial strains were first utilized to ensure a sharp Mott transition, which is required to achieve precise and highly reversible control of the switching property. Generally, epitaxial VO_2 thin films grown on specific surfaces of r-sapphire[23] or rutile TiO_2 single crystals[24,25] have been reported to have a very sharp transition behavior, which was attributed to stress-related modifications of the relative thermodynamic stability of the M1 and R phases, wherein the residual strains can counteract the transition energy barriers and can stimulate the occurrence of the transition sharply, with pixel-by-pixel transition to avoid the effect of intragrain propagation.

However, how heterointerfacial strains affect the Mott phase transition of VO_2 nanoparticles is currently unclear because of the difficulties in the design and preparation of a proper particulate system to manipulate interfacial stresses. However, many interesting scientific problems could be resolved if such particles were available. The objectives of this study were to (i) understand the thermodynamics and kinetics of heteroepitaxy, which is usually unclear in core/shell nanoparticles and (ii) explore the interfacial effect on the Mott phase transition property. To achieve these objectives, VO_2@TiO_2 core/shell nanoparticles with clear heteroepitaxial coherent interfaces were prepared using a sol−gel-based coating method and carefully designed annealing with a relatively slow heating rate under an appropriate atmosphere. An unexpected and unprecedented epitaxial growth of anatase TiO_2 was observed on every faceted VO_2 surface by high-resolution transmission electron microscopy (HRTEM). Such an epitaxial structure can be observed on either the side surfaces of {011} or the end surfaces of {210} in VO_2 (M1). The formation of a local diffusion interface composed of $V_{1-x}Ti_xO_2$ was confirmed by both energy dispersive spectroscopy (EDS) and the analyses of the theoretical misfit and lattice compatibility; this interface is proposed to be the thermodynamically preferable nucleation site for coherent growth. The heating rate was also a critical factor for ensuring the 2-dimensional growth rather than island growth from the kinetic perspective. These nanoparticles exhibit remarkably modulated MST characteristics with respect to the transition temperature and hysteresis width.

By tuning the shell thickness, a designed interfacial stress and Ti-doping can be achieved to yield largely reduced hysteresis. A large strain caused by an ultrathin TiO_2 shell coating on VO_2 can lower the hysteresis from 23.5 to 12.0 °C due to interfacial stress and confinement. Such an interfacial effect can also work well in W-doped VO_2@TiO_2 nanostructures with nearly ambient transition temperatures, suggesting a potential application in energy-efficient windows. The films on glass composed of the as-prepared composite particles exhibited a remarkable solar energy modulation ability and a considerably reduced hysteresis width compared with pure VO_2. Our finding is important both from basic and applied scientific perspectives. The as-obtained nanocomposite particles will benefit future applications of rapid response and high-precision controlling materials, particularly for energy-saving smart windows.

2. EXPERIMENTAL SECTION

2.1. Preparation of VO_2 Nanoparticles. VO_2 nanoparticles with a short diameter of ~50 nm were prepared by hydrothermal treatment of V_2O_5 gel and hydrazine monohydrate (Aladdin) at 260 °C for 24 h as reported in our recent paper.[26] Typically, $V_2O_5{\cdot}nH_2O$ gel was prepared by dissolving 0.3 g of V_2O_5 powder into 10 mL of H_2O_2 solution (5 wt %) in a 25 mL Teflon vessel. Then, the Teflon vessel was sealed in a stainless steel autoclave followed by hydrothermal treatment. After the hydrothermal process, a black−gray precipitate was collected by centrifugation and washed using deionized water and ethanol alternatively three times. The products were dried in a vacuum oven at 60 °C for 6 h. To reduce the phase transition temperature of VO_2, tungsten was used as the cationic substituent element by adding $(NH_4)_{10}W_{12}O_{41}{\cdot}5H_2O$ (Wako, Japan) into the V_2O_5 gel at a designed doping ratio.

2.2. Preparation of VO_2@TiO_2 Core/Shell Nanocomposites. VO_2@TiO_x core/shell particles were first prepared using the sol−gel route. In total, ~0.02−0.05g of the as-prepared VO_2 nanopowders was dispersed ultrasonically in 50 mL of anhydrous ethanol for 15 min. Then, 800 μL of Triton X-100 (Sigma Aldrich) surfactant aqueous solution (0.1M) was added into the suspension and stirred for 2 h. Another stock solution was prepared by dissolving 0.6−1 mL of titanium tetrabutoxide (TBOT, Sigma Aldrich) into 50 mL of ethanol solution under stirring for 10 min. The stock solution was subsequently added into the VO_2 suspension in three steps: 20 mL followed by sonication for 10 min, then 20 mL followed by sonication for 5 min, and finally the remainder of the 10 mL followed by sonication for 5 min. Then, the suspension mixture was aged for 2 h. The product was collected by centrifugation and washed with ethanol twice, and it was finally dried in a vacuum oven for 2 h. To obtain samples with desirable thickness, the synthesis parameters were adjusted including the loading amount of VO_2, the amount of surfactant, and the concentration of TBOT. Details are presented in the Results and Discussion section.

To obtain a crystalline coating, the as-synthesized powders were placed in an alumina crucible and then annealed in a vacuum quartz-tube furnace under a flow of air at specific pressure and temperature. The annealing program was optimized to transform the amorphous shell into crystallized TiO_2 while keeping the VO_2 core chemically intact according to our previous work.[26] Typically, with an air pressure of ~3 Torr, the sample was heated from ambient temperature to 400 °C at a heating rate of ~20 °C/min and then held at 400 °C for 15

min before being naturally cooled to room temperature. To investigate the effect of the heating rate, a more rapid heating process was conducted in a rapid annealing vacuum quartz-furnace with a heating rate of ~80 °C/min.

2.3. Characterizations. X-ray diffraction (XRD) analyses were conducted on a Rigaku Ultima IV diffractometer with Cu Kα radiation (λ = 1.5418 Å) using a voltage and current of 40 kV and 40 mA, respectively. Unless stated otherwise, all the samples were measured at a scanning rate of 3°/min. The microscopic morphology was determined using a field-emission scanning electron microscope (FE-SEM, HITACHI S-3400, Japan) at an acceleration voltage of 15 kV. The microstructure and composition of the samples were further analyzed using a transmission electron microscope (TEM, JEOL2010) with an energy-dispersive spectrometer (EDS) attachment. The Raman spectra of the composite samples were measured using a Raman microscope (Renishaw in Via) with a 514 nm laser source at an input power of 1 mW. This small power was applied to avoid local heating effects.

The first-order phase transition behaviors of the resulting products were measured by differential scanning calorimetry (DSC200F3, NETZSCH) over the temperature range from 0 to 90 °C using a liquid nitrogen cooling unit. The heating and cooling rates were set at 10 °C/min.

The thermochromic properties of the obtained samples were evaluated by coating the powder onto a float glass substrate. For the measurement, a double-sided adhesive and highly transparent Teflon tape was stuck onto the glass substrate in advance. A small amount of the powders was ultrasonically dispersed in ethanol with a solid content of ~3 wt %, and the suspension was uniformly cast onto the Teflon tape, using an automatic bar coating machine, and then dried naturally. The transmittance (T_r) of the film in the wavelength range from 250 to 2600 nm at 25 °C (low temperature M1 phase) and 90 °C (high temperature R phase) was measured using a UV−vis spectrophotometer (HITACHI U-3010) with a integrating sphere and a temperature controlling unit. The transmittance curve of the bare tape-pasted glass was used as a baseline calibration for the transmittance measurements.

3. RESULTS AND DISCUSSION

3.1. Formation and Heteroepitaxy of VO_2@TiO_2 Core/Shell Nanostructure. Sol−gel deposition was used to produce uniform TiO_2 precursor shells onto hydrothermally synthesized VO_2 cores with a controllable thickness ranging from 1 to 7 nm. Detailed experimental parameters for some samples are listed in Table 1. In the $Ti(OR)_4$−H_2O−alcohol (R = $-CH_3$, $-C_2H_5$, $-C_3H_7$, $-C_4H_9$) system,[28,29] $Ti(OR)_4$ is hydrolyzed and then peptized into titania colloids by condensation. Figure 1 presents SEM and TEM images of the morphology of the as-prepared core−shell particles N1−N3 with different thicknesses. The TiO_2 precursor shell was coated onto the VO_2 surface with great thickness uniformity. The thicker titania shells tend to assemble by neck-connecting because of the decrease in heterogeneous nucleation sites.[27]

Table 1. Experimental Parameters for Samples N1−N3

sample no.	VO_2 mass (g)	surfactant aqueous solution[a] (μL)	TBOT/ethanol conc.[b] (mL/L)	thickness[c] (nm)
N1	0.05	800	620	1
N2	0.04	800	620	3
N3	0.03	800	620	7

[a]Amount of surfactant aqueous solution (0.1 M in water) added for 100 mL of suspension. [b]50 mL of TBOT/ethanol solution of various concentrations was added into 50 mL of a VO_2/ethanol suspension. [c]Coating thicknesses were evaluated from TEM and SEM measurements.

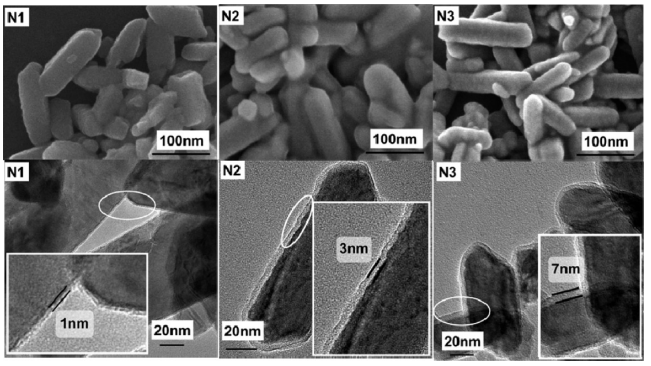

Figure 1. Morphology of VO_2@TiO_2 precursor core/shell particles. SEM images (top row) demonstrated a gradually increased roughness for thicker coatings. The shell thickness can be estimated from the TEM images (bottom row) below to be 1, 3, and 7 nm for samples N1, N2, and N3, respectively.

From the clear contrast between the crystallized VO_2 and the amorphous titania precursor shell, the shell thickness can be roughly estimated to be 1, 3, and 7 nm for samples N1, N2, and N3, respectively.

To obtain a crystalline coating, the annealing procedure was carefully controlled because of the easy oxidation of VO_2 in air or oxygen-rich atmospheres at relatively high temperatures. For obtaining the crystallization of titania while keeping the VO_2 core intact, the composite samples were annealed at the optimized temperature and air pressure of ~400 °C and ~3 Torr, respectively, with a moderate heating rate of 20 °C/min according to our recent work.[26] For phase confirmation of the shell coating, XRD and Raman analyses were utilized. For N1 and N2, only XRD peaks for VO_2 (M1 phase, JCPDF card No.82-0661) can be observed (Figure 2a). The anatase (JCPDF card No. 21-1272) peak can only be clearly identified in sample N3, which possessed the thickest shell. However, the Raman spectra (Figure 2b) indicate that the amorphous TiO_2 shell was crystallized to form anatase; the Raman shift at 143 cm^{-1} can be attributed to the dominating E_{g1} vibration mode in anatase TiO_2.[30] The other peaks denoted by black lines can be attributed to the vibration modes in VO_2 (M1).[17] HRTEM and EDS analyses further confirmed the formation of an anatase shell, which will be discussed below.

After annealing, the core/shell interface became obscure (Figure 3, insets), indicating that the shell coating crystallized with a relatively rough morphology. Lattice-resolved HRTEM images demonstrated that N1, with a shell thickness of 1 nm, did not exhibit clear lattice fringes, indicating poor crystallinity. In contrast, for samples N2 and N3, which possessed much thicker shells, distinguishable crystallographic lattice fringes were clearly observed, and the lattices were identified as being coherently bounded to the VO_2 side faces. Two distinctly different lattices for VO_2 and TiO_2 can be observed, with nearly orthogonal and oblique crossing patterns (schematically illustrated in the rectangular region), respectively. The results indicate that there is a coupled interface between the VO_2 and TiO_2 phases, with the VO_2 core surface serving as propitious sites for the heterogeneous nucleation of the TiO_2 phase. EDS analysis with a beam spot size of less than 1 nm was applied on the shell coating, and the results are presented in the lower-left corner insets of Figure 3. Both V and Ti were detected to coexist in the shell, indicating some degree of Ti−V diffusion in

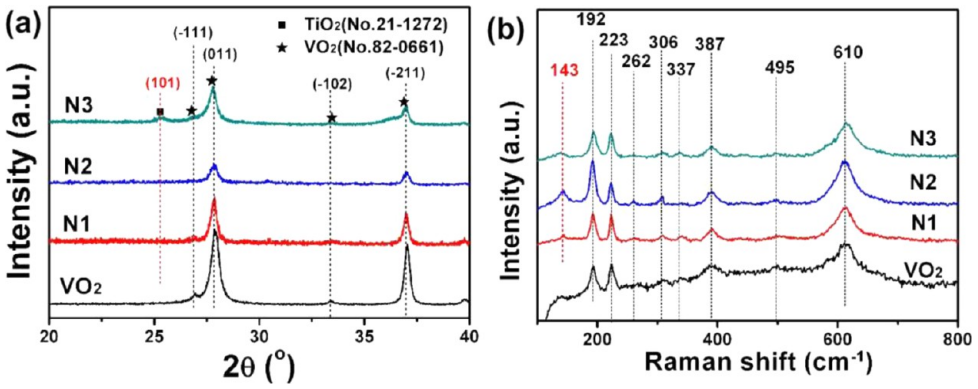

Figure 2. Confirmation of the phase and composition of titania shell by XRD (a) and Raman spectra (b). The Raman spectra indicate that the shell coatings in all the composite samples were crystallized into the TiO_2 anatase phase; however, the XRD peaks for the anatase phase can only be identified in N3, perhaps because of the rather thin coatings in N1 and N2.

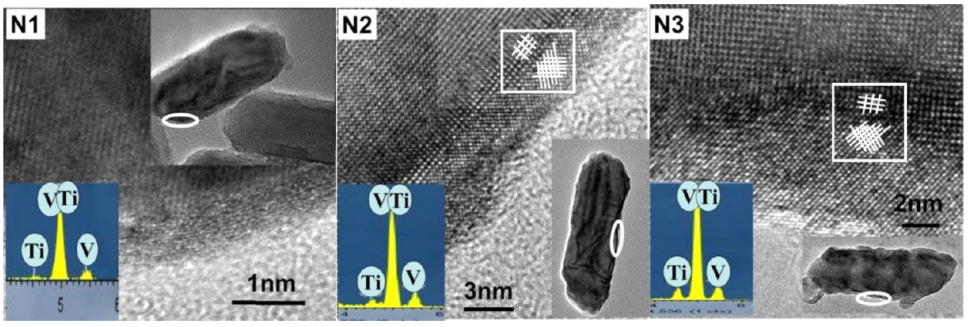

Figure 3. Lattice-resolved HRTEM images for VO_2@TiO_2 core/shell nanoparticles N1, N2, and N3, magnified at the marked part of the rods. The incidental electron beam was adjusted to obtain the best core/shell lattice resolution. The left-bottom corner images present the EDS analysis results for the shell.

the core/shell interface, which might be due to the infinite solubility of Ti in a VO_2 lattice.[28]

We examined the sample N3 in more depth to clarify the epitaxial relationship between the TiO_2 shell and the VO_2 core. In Figure 4a, the 2-dimensional Fourier transform (FT) images of the HRTEM lattice for three different parts (represented by shadow squares) are presented in insets a1−a3. For the VO_2 (M1) core (part 3), the FT image can be indexed to be the reciprocal lattice along the [1−22] zone axis, with the lattice fringes corresponding to the (20−1) and (0−1−1) planes with a crossing angle at 89.6° (the theoretical angle was 89.8° for the bulk crystal). Meanwhile, the FT image for the anatase shell (part 1) can be well indexed to be along the [−201] zone axis with planes (112) and (1−12) obliquely crossed at an angle of 80.2° (slightly larger than the theoretical angle of 78.0°). Notably, the dots representing the (010) and (102) planes disappeared because of the extinction rule in tetragonal symmetry ($h + k + l = 2n + 1$), which conversely confirmed that the TiO_2 lattice is intact and well developed. Meanwhile, the FT images combined with the lattice fringes yielded the following orientation relationship between the anatase shell and the VO_2 substrate:

$$(011)\langle 1{-}22\rangle VO_2(M1)//(010)\langle -201\rangle TiO_2$$

Because the anatase shell is so thin, TiO_2 will account for a considerable part and get distinguishable signal only in the approximation of the core/shell boundary. Therefore, the TiO_2 lattice fringes can be observed only vaguely and almost disappear in the other part of the nanorod far away from the interface. Core/shell lattice contrast in certain nanorods with other incidental orientation cannot be well distinguished by HRTEM because of the deviation of the relative orientation. Although the core and shell can be distinguished from their respective lattice fringes and FT images, the interface is far from sharp as in Si/Ge heteroepitaxial core/shell nanowires[29] or other classical epitaxial multilayered films.[30] Before annealing, the side faces of VO_2 were straight and flat (Figure 1), whereas after annealing the boundary line was kinked along the core/shell interface. As shown in Figure 4a, the FT image of the interface region (Part 2) exhibits an interim pattern that includes part of the TiO_2 lattice along the [−201] axis as well as that of VO_2 along $[1{-}22]_{M1}$. This finding may indicate that the TiO_2 was epitaxially grown onto the VO_2 by first forming an intermediate transition interface. Such a diffusion interface has been frequently designed in other systems[34,35] to serve as a buffer layer to diminish the misfit energy. The interface is composed of a nonuniformly distributed sublattice boundary and steps. Multiple types of defects (vacancies, dislocations) can be observed at the very site of two connected V−Ti atomic planes, revealing a mismatched heteroepitaxy. At the interface, the TiO_2 plane (010) (red dashed curves) makes a subtle, small angle of 1.5° with the VO_2 plane (011) (blue dashed curves). Such a small angle boundary has been reported to appear for heteroepitaxial semiconducting interfaces[31] to relax the high misfit interfacial energy.

Because the heteroepitaxial growth was first observed on the side surface $\{011\}_{M1}$ of VO_2, it is important to survey whether such a heteroepitaxial relationship is only limited to these specific planes. The SEM images reveal that the geometrical shape of the VO_2 powders is a nanorod structure with a long-

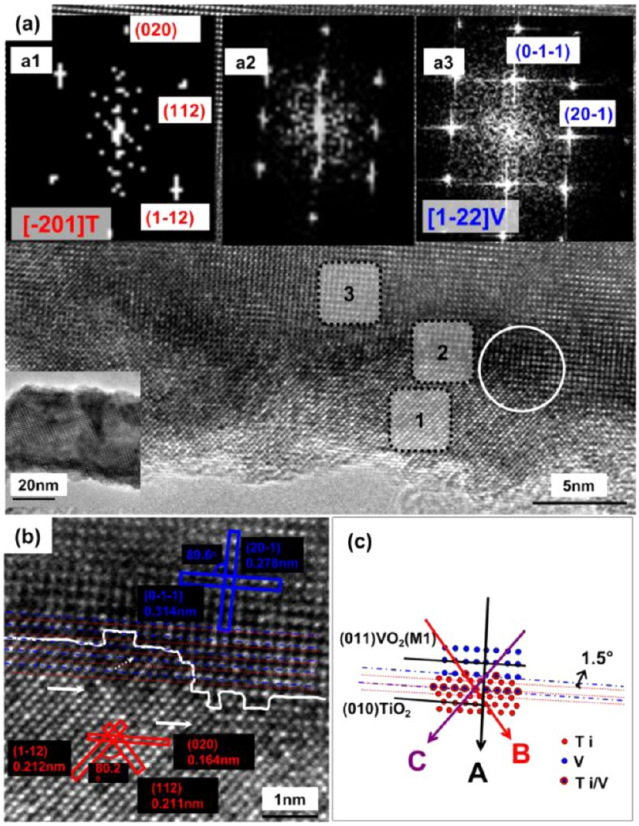

Figure 4. Interfacial orientation relationship between the VO_2 core and TiO_2 shell. (a) HRTEM image for the bottom part of a rod from sample N3. Insets a1, a2, and a3 are the fast Fourier transform images for the corresponding shadow parts indicated by the square dotted boxes. (b) The magnified circular part at the bottom right corner of a, and the epitaxial relationship can be clearly identified. The labeled lattice fringes correspond to the different interplanar distances for the lattice planes (blue and red represent VO_2 and TiO_2, respectively), and the interfacial line is denoted by a white broken line. The dashed and solid arrows indicate the defect sites of vacancies and dislocations. (c) Schematic illustration of the interfacial relationship between the dense TiO_2 lattice (red) and the relatively loosely packed VO_2 lattice (blue) wherein an approximate orientation relationship can be made: (011) VO_2 (M1) // (010) TiO_2. Atomic substitution or diffusion can be expected and represented by the possible occupation of Ti or V on the interfacial plane. Three arrows A, B, and C suggest the possible direction for initial epitaxial growth.

radius ratio no higher than 10, mainly because of the preferential growth along the a_{M1} axis[37,38] Here, a single nanorod was analyzed by HRTEM with four faceted faces, including two side faces and two end faces, and the images were presented in Figure 5. The shape of the ends was such that the nanowire grows in a direction that forms an acute angle of 45° with the end surfaces S3 and S4. Two parallel side surfaces (Figure 5, S1 and S2) were coated by the epitaxial TiO_2 shell with the same orientation relationship as discussed in Figure 4: (011) ⟨1−22⟩ VO_2 (M1) // (010) ⟨−201⟩ TiO_2. In particular, for the end surfaces, epitaxially grown TiO_2 shells can also be observed at the interface (Figure 5, S3 and S4). The end faces were identified to be $\{210\}_{M1}$ planes, with relatively larger in-plane lattice parameters than that of the side surface $\{011\}_{M1}$. The {210} end planes were theoretically calculated to form an acute angle of 45.7° with the rod axial $[100]a_M$ direction, which is in accordance with the observation. This result implies that

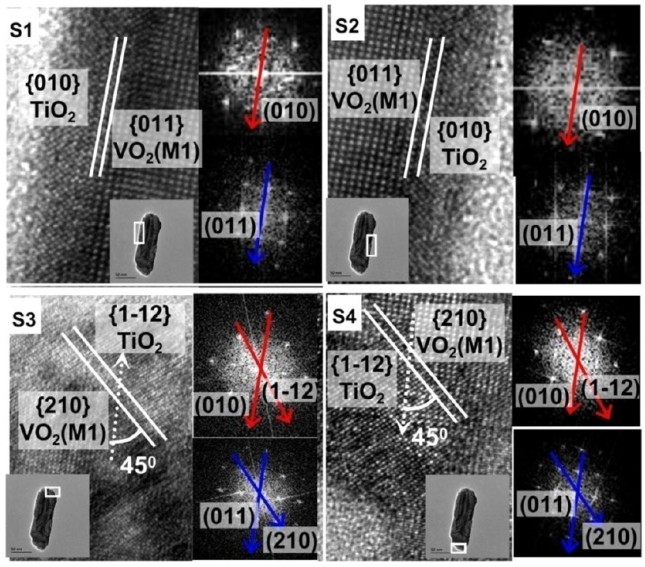

Figure 5. Scrutiny of the epitaxial relationship on every faceted surface of a single VO_2/TiO_2 rod (N2). S1 and S2 are the left and right side surfaces, and S3 and S4 are the upper and bottom end surfaces. Fourier transform images are shown on the right part, with the upper and bottom insets corresponding to the TiO_2 and VO_2 lattices, respectively. For side surfaces S1 and S2, an orientation relationship is clearly evidenced as: {011} VO_2 (M1) // {010} TiO_2; whereas on the two end surfaces S3 and S4, the exposed plane of VO_2 is $\{210\}_{M1}$, wherein another orientation relationship can be deduced as: {210} VO_2 (M1) // {1−12} TiO_2. The solid and dashed white curves indicate the interfaces and the rod axial directions, respectively.

TiO_2 is not limited to only coherent growth on VO_2 $\{011\}_{M1}$ but can also grow on other faces, such as $\{210\}_{M1}$. Most surprisingly, the epitaxial orientation relationship on the $\{210\}_{M1}$ faces is identified to be the same as that on the $\{011\}_{M1}$ planes. The FT image for the TiO_2 shell can also be indexed to be the reciprocal lattice along the [−201] zone axis, with the (010) planes also approximately parallel to the (011) plane of VO_2 (Figure 5, S3 and S4). Such a consistent orientation relationship for epitaxial growth on all of the planes ensures the formation of a nearly intact and continuous TiO_2 shell.

3.2. Epitaxial Growth Mechanism. For the study on epitaxial growth, it is straightforward to reverse-trace the growth process based on the above discussion. With respect to the VO_2 $(011)_{M1}$ plane, there are three possible directions for TiO_2 to epitaxially nucleate on VO_2, as illustrated in Figure 4c. Notably, when TiO_2 begins to grow on VO_2, VO_2 is in its metallic state (∼ 400 °C) with a tetragonal rutile structure, which is further denoted as VO_2 (R). Therefore, focus should be cast on the epitaxial relationship between the specific planes of VO_2 (R) and TiO_2. Along direction A marked by the black arrow (Figure 6a), the VO_2 $(110)_R$ and TiO_2 (010) planes are the growing planes. On these two planes, the TiO_2 (anatase) holds an epitaxial orientation relationship as (010) ⟨−201⟩ TiO_2 // (110) ⟨−110⟩ VO_2 (R), with another (010) ⟨301⟩ TiO_2 // (110) ⟨001⟩ VO_2 (R) relationship in their respective perpendicular directions, and the crossing angles of the in-plane directions for TiO_2 (010) and VO_2 $(110)_R$ are 88.5° and 90°, as indicated in the bottom crystallographic structure of Figure 6a. The other red and purple directions are crystallographically identical in VO_2 (R) because [−110] is the 4-fold rotational symmetric axis. Here, only the red direction B was considered.

dx.doi.org/10.1021/am401297g | ACS Appl. Mater. Interfaces 2013, 5, 6603−6614

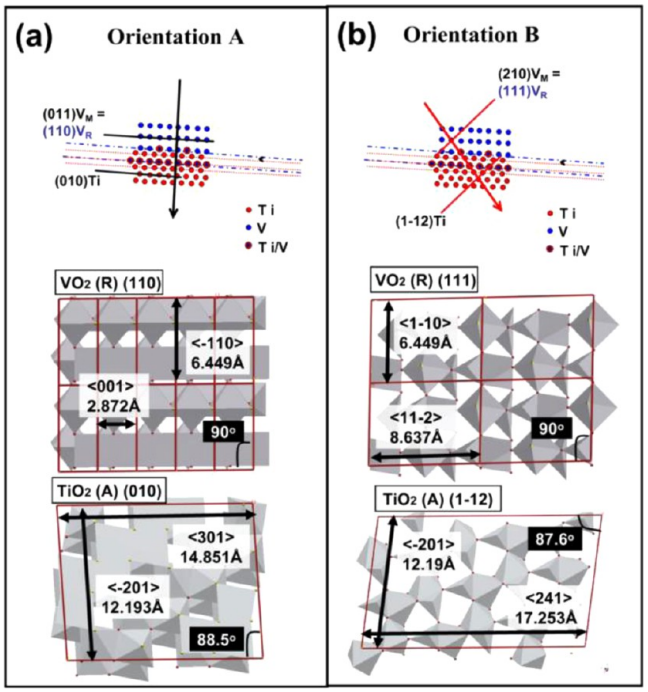

Figure 6. In-plane lattice orientation relationship between VO_2 and TiO_2 based on two different epitaxial orientations A and B. The lattice parameters for VO_2 (R) and TiO_2(anatase, A) were taken at 400 °C based on the literature.[39,40] The growing planes for VO_2 and TiO_2 are schematically depicted in polyhedral crystallographic structures, and the corresponding lattice parameters are labeled accordingly.

For the red direction B (Figure 6b), the VO_2 $(111)_R$ (corresponding to the end $(210)_{M1}$ surface of S3 and S4) and TiO_2 (1−12) planes were the growing planes. In this case, the TiO_2 (anatase) has an epitaxial orientation relationship as (1−12) ⟨−201⟩ TiO_2 // (111) ⟨1−10⟩ VO_2 (R), with another (1−12) ⟨241⟩ TiO_2 // (111) ⟨11−2⟩ VO_2 (R) relationship in the respective perpendicular direction. For the above two directions, the lattice misfit can be calculated using the formula: $\delta = (ma_{TiO2} - na_{VO2})/ma_{TiO2} \times 100\%$, in which δ is the relative lattice misfit, a_{TiO2} and a_{VO2} denote the lattice parameters in the specific growing plane for TiO_2 and VO_2, respectively, and m and n represent the matching of integral multiples of lattice planes between them because of the different periodicity.

Considering the lattice expansion during heating, the different lattice parameters at ambient temperature (25 °C) and growing temperature (400 °C) for both VO_2 (M1 phase at 25 °C and R phase at 400 °C) and TiO_2 were utilized[40,41] in our misfit calculation. Additionally, the intersection angle between two lattice vectors will also change because of the anisotropic lattice expansion. However, such a change is rather small after calculation. Specifically, the planar orientation relationship and the calculated misfit are summarized in Table 2, both for the high-temperature VO_2 (R) phase and the room-temperature VO_2 (M1) phase. For direction A, the lattice misfits along two nearly orthogonal directions are 3.31% and −5.78%, respectively. However, for the direction B, the misfit is relatively larger, 11.23% and −5.78% for the two orthogonal directions, respectively, revealing that the planes normal to direction A are more energy-preferable for TiO_2 nucleation and subsequent epitaxial growth (for a detailed misfit calculation, please refer to Supporting Information S1).

Herein, a misfit on such a scale (3.31%∼11.23%) can ensure that the two crystals are coherently matched with a relatively moderate interfacial misfit energy.[34,36,42] However, the atomic configuration and the [MO_6] octahedral connection profile on these 2-dimensional planes are hardly the same. The TiO_2, which has a considerably longer periodicity, cannot simply coherently grow on the VO_2 surface without other energy-preferable nucleation centers. In this premise, a indirect step-flow heteronucleation growth mechanism[32] can be deduced and described as follows: primarily, the adsorbed Ti species ($TiO_y(OH)_m(OR)_q$) were thermally activated and Ti atoms/clusters were diffused into the VO_2 lattice, forming a local $Ti_xV_{1-x}O_2$ solution oxide with some V sites substituted by Ti. This process can conversely support the defect-rich and obscure interface as previously presented. Such a diffusion/substitution was made possible at 400 °C, which has been frequently reported,[12,44] because Ti was reported to have infinite solubility in a VO_2 lattice. The resulting $Ti_xV_{1-x}O_2$ solution ($0 < x < 0.2$) also exhibits a MS transition from the tetragonal to monoclinic structure. With x ranging from 0 to 1, the lattice parameters gradually and continuously changed from those of VO_2 to those of TiO_2 (rutile). The lattice parameter and bonding length were more approximate to TiO_2, which can reduce the lattice misfit and serve as a more preferable nucleation site to favor subsequent epitaxial growth. Thermodynamically, the decrease in the Gibbs free energy, $\Delta G = \Delta G^\circ + (\gamma_{TiO2} + \gamma_{TV} - \gamma_{VO2})$, is the driving force for epitaxial growth in that system. Here, $\Delta G^\circ = \Delta H - T\Delta S$ denotes the internal part for TiO_2 crystallization and $(\gamma_{TiO2} + \gamma_{TV} - \gamma_{VO2})$ represents the surface/interface energy change. The diffused layer and well-matched lattice largely reduced the interfacial energy γ_{TV}, thus favored epitaxy. Anatase TiO_2 has been reported[33] to transform into the rutile phase at 600−700 °C under ambient

Table 2. Summary of the Theoretical Misfit δ of TiO_2 (Anatase) on VO_2 along Directions A and B[a]

coating/substrate	in-plane angle	epitaxial relationship	periodic lattice parameter (Å)	misfit δ (%)
TiO_2/VO_2 (R) @400 °C (direction A)	88.5°/90.0°	(010) ⟨301⟩ TiO_2 // (110) ⟨001⟩ VO_2 (R)	(14.851)/(2.872 × 5)	3.31
		(010) ⟨−201⟩ TiO_2 // (110) ⟨−110⟩ VO_2 (R)	(12.193)/(6.449 × 2)	−5.78
TiO_2/VO_2 (M1) @25 °C (direction A)	88.5°/89.8°	(010) ⟨301⟩ TiO_2 // (011) ⟨100⟩ VO_2 (M1)	(14.811 × 2)/(5.753 × 5)	2.89
		(010) ⟨−201⟩ TiO_2 // (011) ⟨1−22⟩ VO_2 (M1)	(12.158)/(12.814)	−5.40
TiO_2/VO_2 (R) @400 °C (direction B)	87.6°/90.0°	(1−12) ⟨−201⟩ TiO_2 // (111) ⟨1−10⟩ VO_2 (R)	(12.193)/(6.449 × 2)	−5.78
		(1−12) ⟨241⟩ TiO_2 // (111) ⟨11−2⟩ VO_2 (R)	(19.460)/(8.637 × 2)	11.23
TiO_2/VO_2 (M1) @25 °C (direction B)	81.9°/82.2°	(1−12) ⟨−201⟩ TiO_2 // (210) ⟨1−22⟩ VO_2 (M1)	(12.157)/(12.814)	−5.40
		(1−12) ⟨241⟩ TiO_2 // (210) ⟨1−2−2⟩ VO_2 (M1)	(19.413)/(17.253)	11.13

[a]The lattice parameters were calculated with consideration of thermal expansion at 400 °C. The misfit was calculated using the following formula: $\delta = (ma_{TiO2} - na_{VO2})/ma_{TiO2} \times 100\%$, in which a_{TiO2} and a_{VO2} represent the matched lattice parameters as indicated in the third column and m and n represent the matching of integral multiples of lattice planes between them because of the different periodicity.

pressure, which has greater lattice compatibility with the rutile VO_2 (R) phase. However, such a high temperature will ruin the original structure of VO_2. Therefore, in the temperature range in question (~400 °C), the anatase is thermodynamically more preferred to form than rutile phase. The possibility for epitaxial growth was derived from both the well-matched lattice in the above-discussed planes and the heteronucleation thermodynamic requirement in such a thin shell.

According to the theory predicted by the Matthews-Blakeslee model[34] in heteroepitaxy, there should be a critical shell thickness, above which the dominating 2-dimensional growth will evolve to 3-dimensional island-like growth, when the misfit strain energy cannot be relaxed by forming dislocations. As reported in our previous work,[26] VO_2@TiO_2 microrods (diameter $\varphi \sim 500$ nm) with shell thickness larger than 20 nm will form a polycrystalline island-like anatase shell (also see Supporting Information S2). This finding indicates that, when the thickness reaches far beyond the critical value, the misfit strain can not be maintained by the formation of misfit dislocations but must be relieved by forming polycrystalline boundaries.

In addition to the shell thickness, the heating rate also exerts a significant effect on the growing mode from kinetic considerations. For the titania coated composite samples N2 and N3, when the heating rate is increased to 80 °C/min (this rapid annealing was conducted in a RTA vacuum furnace), spherical particulate TiO_2 anatase was formed on the core surface in an island mode rather than a compact epitaxial one (Figure 7). This finding is the natural result of the kinetic competition between 3-dimensional nucleation and lateral diffusion along the surface of VO_2. When the heating rate is rather high, nucleation dominates and favors single particulate growth.

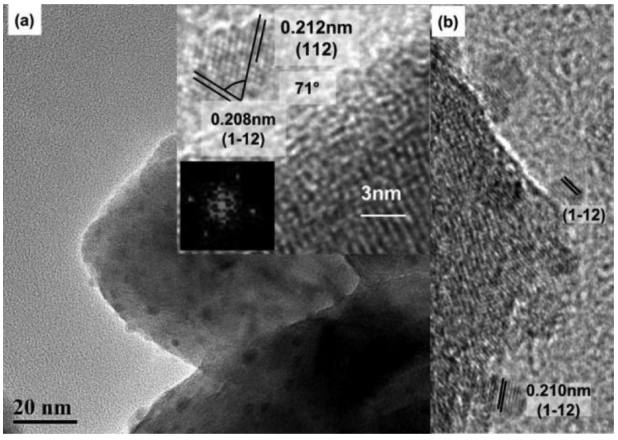

Figure 7. TEM images for sample N3 after annealing at a rapid heating rate (80 °C/min). (a) Nearly spherical anatase particles were observed to grow discretely on the VO_2 surface. Inset figure: the lattice fringes for the spherical TiO_2 can be indexed to the (112) and (1−12) planes of anatase with an intersection angle of 71° (the theoretical angle is 76°). Left-bottom: fast Fourier transform image corresponds to the 2-dimensional HRTEM lattice of the spherical anatase. (b) Another part of the sample surface; particulate anatase grains can also be identified.

3.3. Effect of Interface Epitaxy on the Mott Phase Transition. For our core/shell nanocomposites, the effect of interfacial strain induced by the epitaxial ultrathin shell can be naturally expected, which enables explorations of the possibility of using interfacial strain to modify Mott phase transition properties in VO_2 powders. Here, the ferroelastic first-order structural phase transition was first investigated and discussed.

The first-order phase transition of VO_2 powders was investigated by monitoring the enthalpy change using DSC analysis, and the results are presented in Figure 8 and summarized in Table 3. After annealing, all the composite samples exhibited an increased transition temperature (T_c) in both the heating and cooling cycles, although detailed values varied for different samples: 73.8 °C (heating)/54.8 °C (cooling) for N1, 76.8 °C (heating)/ 63.9 °C (cooling) for N2, and 77.6 °C (heating)/65.6 °C(cooling) for N3, respectively, representing a T_c increase of 8.3−12.1 °C in the heating cycle and 12.8−23.6 °C in the cooling cycle compared with unannealed pure VO_2. Meanwhile, the width of the hysteresis loop (ΔT_c, the difference of the T_c in the heating and cooling cycles) of N1, N2, and N3 was reduced after annealing from 23.5 to 19.0, 12.9, and 12.0 °C, respectively. Furthermore, the enthalpy change (for unit mass) during the transition was gradually reduced with increased coating thickness. This result can be naturally expected because TiO_2 does not exhibit a phase transition in this temperature range. Note that, for real applications, the transition temperature can be easily tuned by doping with W. In fact, W-doped samples (further denoted as VO_2:W) were also prepared with a W-doping content of ~1.34 atom % (preparation and TEM images are presented in Supporting Information S3). After the anatase coating, the VO_2:W @TiO_2 particles also exhibited a similarly modified phase transition temperature, as depicted in Figure 8b, with the hysteresis reduced from 24.1 to 14.7 °C, demonstrating the potential to obtain a practically applicable sharp switching smart window with a near ambient transition temperature. Notably, the ΔH for VO_2:W@TiO_2 is slightly higher than that for VO_2:W, mainly due to the diminished defect concentration caused by high-temperature structural relaxation.

In general, the ferroelastic transition[46,47] between the semiconducting M1 phase and the metallic R phase primarily includes two processes: the nucleation of a new phase in the original phase matrix and the boundary/domain wall diffusion of the heterophase (M1&R). The nucleation is thermodynamically activated, which primarily depends on the microstructure (structural or chemical defects, where nucleation always preferentially initiates). The activation energy for the phase transition in VO_2 was reported to be ~0.5−1 eV;[35−37] therefore, heterogeneous nucleation dominates the initial nucleation process rather than homogeneous nucleation by thermal activation ($\sim k_BT$ = 0.03 eV). The introduction of electronic or structural defects can change the transition temperature and hysteresis loop width by tuning the activation energy. After annealing, the elevated T_c indicates that the chemical stability of the M1 phase has increased with a larger activation energy for the phase transition to the R phase.

The microstructural change caused by the mismatched interface plays a deciding role in decreasing the hysteresis width. Such a structural change was corroborated by the main diffraction peak shift of VO_2 (M1) (011) using slow-scanning XRD (scanning rate of ~1°/min), as plotted in Figure 9a, revealing a (011) interplanar expansion. Meanwhile, a large degree of lattice compression of TiO_2 in the {010} and {201} planes was also confirmed by statistical measuring of the planar distances from the HRTEM images (Figure 9b), suggesting that a large tensile stress was applied to TiO_2 via the vertical direction against growing plane. That result is in accordance with the expansion in the VO_2 lattice along the $(110)_{M1}$ ⟨100⟩

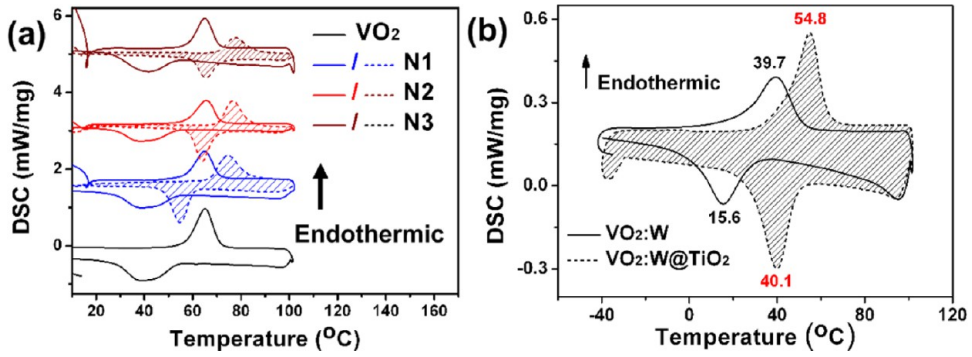

Figure 8. First-order phase transition property of the as-prepared VO_2@TiO_2 nanocomposites by DSC analysis. (a) DSC curves for pure VO_2 (black curves) and samples N1 (blue curves), N2 (red curves), and N3 (claret curves) before (solid curves) and after annealing (dashed curves with shadow filling). (b) DSC curves for VO_2:W powders (solid curves) and VO_2:W @TiO_2 powders (dashed curves).

Table 3. Summary of the Transition Temperature and Change of Enthalpy (ΔH)[a]

		T_c_DSC (°C)		
	ΔH (J/g)	heating	cooling	ΔT_c
VO_2	46.77	65.5	42.0	23.5
N1_an	44.94	73.8	54.8	19.0
N2_an	37.65	76.8	63.9	12.9
N3_an	24.49	77.6	65.6	12.0
VO_2:W	22.01	39.7	15.6	24.1
VO_2:W@TiO_2	29.50	54.8	40.1	14.7

[a]"_an" denotes the sample after annealing. ΔH for different samples was calculated from the value of the integrated area for the endothermic peak during heating.

direction. The local stress in the interface formed distorted defective sites, which lowered the activation energy for phase transition; thus, the requirement on the supercooling degree for the phase transition from R to M1 was diminished.[38] Unlike epitaxial films grown on substrates, susceptible deformation and a considerable part of the elastic energy can be expected in the core material.[39] Another important difference between planar substrates and nanorods is that, due to their large surface-to-volume ratio, the morphological instability of the core−shell nanorods critically depends on the surface stress. In comparison with VO_2, TiO_2 has a much stiffer lattice (with a larger Young's modulus); therefore, the lattice change of TiO_2 can be viewed as strong evidence that the VO_2 core was largely deformed by interfacial strain, which is consistent with our previous theoretical calculations on misfit. The misfit on the side surface of the rod will most likely induce substantial lattice deformation along the rod growing direction $[100]_{M1}$ (c_R axis) in a periodic profile.

Here, the deformation along c_R (corresponding to a_{M1}) was critically important, because the unaxial stress/strain along c_R can exert a significant effect on the transition property as previously introduced. From the location of the (011) peaks, the respective variation of $d_{(011)}$ compared with pure VO_2 can be calculated and taken as the same with the relative lattice change in a_R, for the corresponding relationship: $d(011)_{M1} \approx d(110)_R = (2)^{1/2} a_R$. For the $\{001\}_R$ plane, the change in the in-plane lattice parameter δab for samples N1, N2, and N3 was calculated to be 0.254%, 0.454%, and 0.218%, respectively. The change in the out-of-plane lattice parameter δc was calculated from the Poisson ratio ν ($\nu = 0.3$)[24] to be −0.076%, −0.136%, and −0.065%, respectively. In addition to the residual strain, the mismatch in the thermal expansion coefficient can also be inflential. The average linear expansion coefficient (100−480 °C)[40] is 25×10^{-6} K^{-1} for VO_2 along c_R and 4.5×10^{-6} K^{-1} along a_R, whereas the values for titania[41] are 7.38×10^{-6} K^{-1}

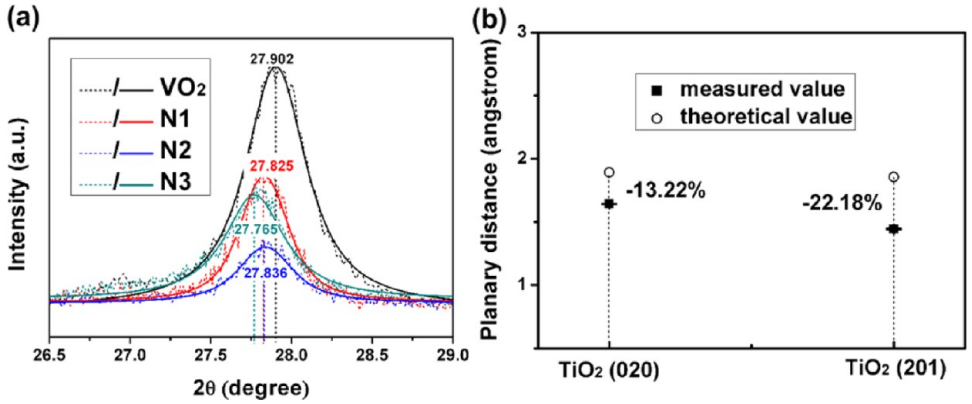

Figure 9. Investigation of the structural change after annealing. (a) XRD slow scanning curves from 26.5° to 29.0° (peak of $(110)_{M1}$) for VO_2 (black) and annealed N1 (red), N2 (blue), and N3(green); the clear peak shifts indicate that the crystallographic structure changed after annealing. The XRD peaks were fitted by Voigt functions, and smooth fitted curves are also presented. (b) The planar distances {020} and {201} of anatase TiO_2 in sample N3 from a statistical analysis of the HRTEM lattice fringes on 20 rods, with every measurement taken no less than 10 times in a single rod shell (the distances were measured using Gatan Digital Micrograph software). Meanwhile, the theoretical planar distances (hollow circles) were also calculated for comparison, and the corresponding respective lattice shrinkage ratio is shown in the figures.

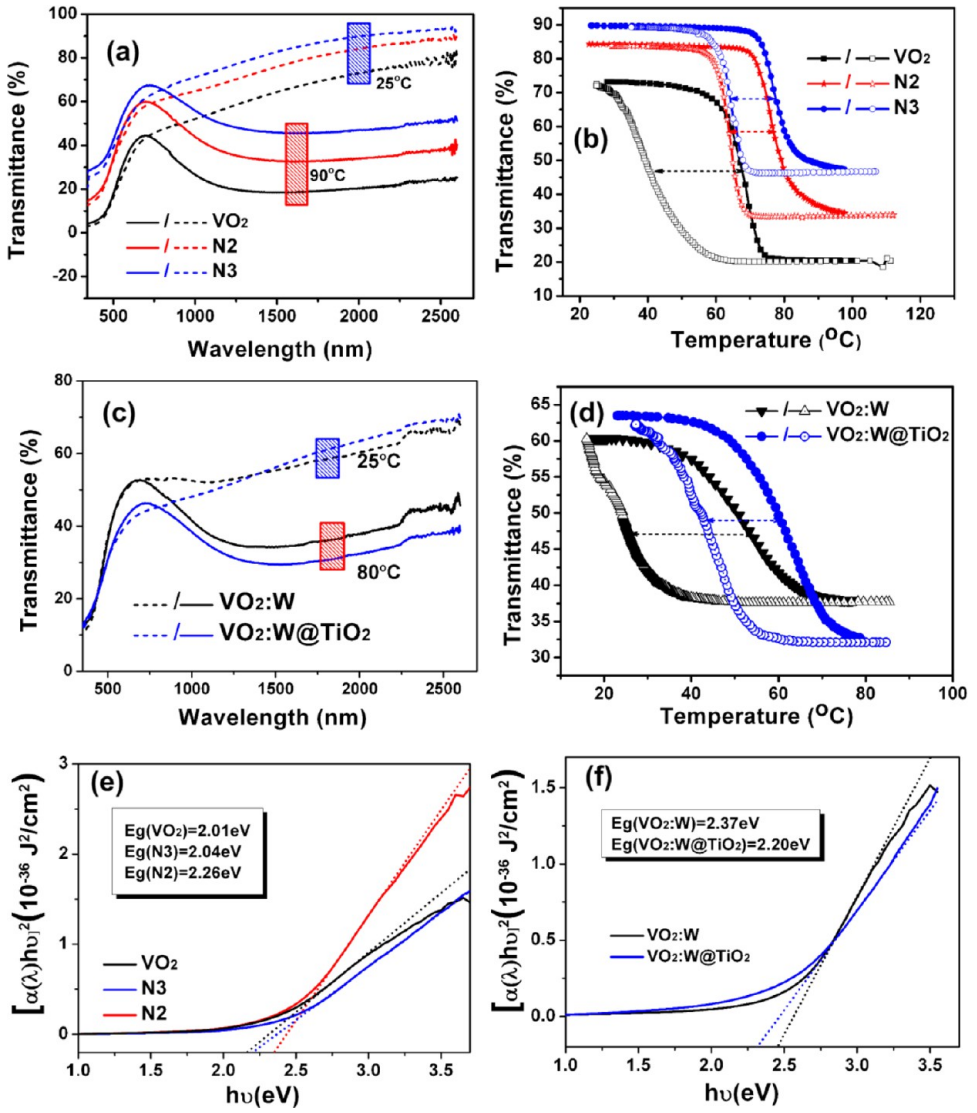

Figure 10. Thermochromic performance of the powder-based films by coating the as-prepared core/shell particles. (a and c) The diffuse transmittance spectra in the UV–vis–near-infrared wavelength range. Samples in (a) are VO_2 (black curves), N2 (red curves), and N3 (blue curves) at 25 °C (dash curves) and 90 °C (solid curves). Spectra for W-doped VO_2 and anatase coated sample are presented in (c). (b and d) The temperature-varied transmittance hysteresis loop plots of the corresponding samples at 2000 nm during heating (solid) and cooling (hollow) cycles. (e and f) Plot of the $(\alpha h\nu)^2$–$h\nu$ relationship; the estimated optical energy band gap was shown.

($a_{//}$) and 3.53×10^{-6} K^{-1} ($a_{\perp}$). This mismatch may result in an expansion (or shrinkage) prevailing along the rod length direction (because c_R[001] corresponds to a_M[100]), which induces a compressive (when heating) and a tensile (when cooling) stress on the VO_2 rod. The thermal stress changed the defect state and contribution on the local surface, which would affect the phase transition behavior of VO_2.

With the exception of long-range compression posed on VO_2, the Ti doping effects at the interface can also play an important role. Here, the EDS results can only confirm that the shell contains a majority of Ti and a small amount of V; however, the poor spatial resolution cannot confirm the thickness of the diffused solid solution layer. Even so, Ti–V interdiffusion in the VO_2@TiO_2 (20 nm) system has been confirmed by scanning TEM in our previous work;[26] together with the observed defect-rich core/shell interface, boundary Ti-doping into VO_2 can be reasonably expected in the present core/shell nanostructure. Titanium (Ti) is the most effective reported doping element for continuously reducing the hysteresis loop width by increasing the Ti content. The reported modulation ability of hysteresis typically occurs at ~9.2 °C/atom %[38] for the sol–gel route, and nearly zero hysteresis can be achieved in polycrystalline $V_{0.86}Ti_{0.14}O_2$ films obtained by metal organic deposition[42] and $V_{0.882}W_{0.018}Ti_{0.10}O_2$ codoped films.[43] The incorporation of Ti favors a heterogeneous nucleation process by forming defects such as Ti substitutions or O vacancies, in which a single domain grain can achieve synchronous grain-by-grain transition. A similar interfacial diffusion and Ti-doping can occur at 400 °C,[44] 450 °C,[12] or 500 °C[38] for TiO_2/VO_2 multilayer films. Ti-doping forms another metastable M2 phase and induces the formation of internal stress, which is reflected in an increase in the Mott phase transition temperature. We should note that Ti-doping only reasonably existed in the core/shell boundary with limitations at only a few atomic layers thick. Therefore, the exact effects of boundary doping on the transition dynamics remain unclear.

dx.doi.org/10.1021/am401297g | ACS Appl. Mater. Interfaces 2013, 5, 6603–6614

Table 4. Summary of Transmittance and Modulation Ability at 2 μm

	integrated solar transmittance T_{sol} (%)[a]			luminous transmittance T_{lum} (%)[c]		
	@25 °C	@90 °C	solar modulation efficiency ΔT_{sol} (%)[b]	@25 °C	@90 °C	hysteresis ΔT (°C)[d]
VO_2	39.72	27.70	12.02	26.75	30.17	21.8
N2	53.63	43.35	10.28	43.34	46.61	13.3
N3	59.31	53.11	6.20	47.52	53.29	13.1
VO_2:W	46.66	40.92	5.74	44.91	45.11	27.6
VO_2:W@TiO_2	41.66	36.15	5.51	36.32	37.68	15.4

[a]The solar transmittance is calculated by such formula: $T_{sol} = \int\varphi(\lambda)T_r(\lambda)d\lambda/\int\varphi(\lambda)d\lambda$, in which $\varphi(\lambda)$ is the solar irradiance spectrum for air mass 1.5 corresponding to the sun standing 37° above the horizon and $T_r(\lambda)$ is the transmittance of our sample.[14] [b]The solar transmittance modulation efficiency was calculated using $\Delta T_{sol} = T_{sol}$@90 °C − T_{sol}@25 °C. [c]Luminous transmittance (T_{lum}) is calculated using the formula: $T_{lum} = \int\varphi_{lum}(\lambda)T_r(\lambda)d\lambda/\int\varphi_{lum}(\lambda)d\lambda$, in which $\varphi_{lum}(\lambda)$ is the relative sensitivity of the human eye in visible light. The integral was aquired from 380 to 780 nm; details are provided in our recent work.[14] [d]Hysteresis (ΔT) was evaluated by the difference of the transition temperature during heating and cooling. Here, the transition temperature was defined as the point when the transmittance arrived at the midvalue between the maximum and minimum value.

From the above discussion, it can be concluded that the phase transition property of the VO_2 core has been largely modified by electronic and atomic reconstructions resulting from vacuum annealing. Long-range mismatch strain and interfacial diffusion jointly led to the change in the phase transition property.

3.4. Thermochromic Performance of Films Coated Using VO_2@TiO_2 Nanoparticles. VO_2 can serve as a potential energy-saving material by smartly modulating the infrared transmittance with varying temperature. The largely reduced hysteresis was significant for achieving practically acceptable energy efficiency. Here, the thermochromic properties of pure VO_2 and VO_2@TiO_2 composites with epitaxial shells (samples N2 and N3) were investigated by coating the powder onto a highly transparent and heat resistant Teflon tape (details are presented in the Experimental Section). For consideration of the roughness of the as-prepared films, UV−vis diffuse transmittance (further denoted as T_r) including the scattering effect spectra were measured at 25 °C (M1 phase) and 90 °C (R phase), and these spectra are presented in Figure 10a. The transmittance hysteresis loop at 2000 nm with various temperatures is presented in Figure 10b. For real applications, W-doped samples with near ambient T_c were also evaluated; the corresponding transmittance spectrum and hysteresis loop are presented in Figure 10c,d. All these samples exhibit conspicuous solar infrared modulability, and the modulation efficiencies and hysteresis are summarized in Table 4.

Neither Teflon tape nor TiO_2 have thermochromic properties; therefore, the change in T_r with temperature should be due to the phase transition of the VO_2 particles. In the near-infrared region, the transmittance at 25 °C is considerably greater than that at 90 °C (so-called IR switching). VO_2 is transparent to IR at lower temperatures (semiconducting M1 phase) and is highly reflective above the T_c (metallic R phase). The plasma frequency (ω_p) for the R phase in polycrystalline thin films has been reported to be 1.0 eV (~1.24 μm)[45] or 1.6 eV (~775 nm);[46] thus, the metallic R phase has a lower transmittance and higher reflectance in the IR region ($\omega < \omega_p$). However, semiconducting VO_2 (M1) has a band gap at approximately 0.6−0.7 eV; therefore; it is highly transparent to photons with energies less than E_g ($\lambda > \sim 1.77$ μm). Considering that the IR part composes over 40% of the total solar energy spectrum, the solar energy can be substantially modulated. Here, the integrated solar energy transmittance (T_{sol}) was calculated, and the difference of T_{sol} between high and low temperatures was used to evaluate the solar modulation efficiency (detailed calculation procedure is presented in the Table 4).

In particular, the TiO_2-coated composite film exhibited a modified optical switching property, both in the hysteresis loop width and the modulation level. The TiO_2 coating can significantly reduce the transition hysteresis width to 13.3 and 13.1 °C for samples N2 and N3 compared with pure VO_2 (21.8 °C) and from 27.6 to 15.4 °C for W-doped samples, which is consistent with the DSC measurements. Films prepared using powders in previously reported studies commonly exhibited a very wide hysteresis. In an earlier work, we prepared films based on VO_2 nanoparticles with large hysteresis[47] (~21 °C) and VO_2@SiO_2 composite particles with a very wide transition range[14] (~30 °C). Lu et al.[48] prepared a VO_2/PEGDA film with a hysteresis width of ~25 °C. Large hysteresis will lead to an unresponsive phase transition and reduce the ultimate energy-saving efficiency. Our composite particles with considerably reduced hysteresis will benefit future applications for rapidly responding and high-precision controlled materials, especially for energy-saving smart windows. For the composite films, the solar modulation efficiencies were 10.28% and 6.20% for N2 and N3, respectively, indicating a degree of efficiency deterioration compared with the pure VO_2 film (12.02%), which is mainly attributed to the defects induced by Ti doping[44] and the reduced portion of VO_2 per unit area. However, the significantly reduced hysteresis may compensate for this weakness, and further optimization in the VO_2 size and coating thickness will benefit better integrated performance. In particular, after being coated with highly transparent TiO_2, the composite films exhibited an improved luminous transparency. As indicated in Table 4, samples N2 and N3 with TiO_2 coatings exhibited significantly increased luminous transmittance by 16% and 22%, respectively, in comparison with pure VO_2. The transparent TiO_2 coating accounts for a considerable part of the total film in the composite samples, which will increase the total visible transmittance.

Furthermore, TiO_2 coating not only narrowed the hysteresis but also changed the optical band gap of the material (Figure 10e,f). The absorption coefficient α was evaluated using Beer−Lambert's law,

$$\alpha d = -\ln\left(\frac{T}{1-R}\right) \quad (1)$$

and the optical band gap, E_g, was determined using the linear extrapolation of $(\alpha h\nu)^2$ vs $h\nu$ near the band gap providing E_g as the intercept at the $\alpha = 0$ axis with the following formula:

$$(\alpha h\upsilon)^2 = A(h\upsilon - E_g) \quad (2)$$

For undoped samples, TiO_2 coating can lead to the blue shift from 2.01 eV in pristine VO_2 to 2.04 eV (N3) and 2.26 eV (N2); whereas for W-doped samples, a red shift from 2.37 to 2.20 eV was found after TiO_2 coating. The change in E_g reflected the nature and the concentration of the defects. For N2 and N3, the incorporation of Ti and the interfacial stress induced a blue shift, owing to the increasing concentration of defects. For W-doped VO_2, the TiO_2 coating and vacuum annealing will dominantly reduce the concentration of the internal defect by structural relaxation, which cannot counteract the blue shift effect of interfacial stress. Such a result is in accordance with the increased enthalpy change and enhanced solar modulation ability.

4. CONCLUSIONS

VO_2 can be heteroepitaxially coated with anatase TiO_2, which has a different symmetry compared to VO_2. The interfacial strain has a pronounced effect on the Mott phase transition when using core/shell nanotechnology. A TiO_2 ultrathin shell with the anatase phase can be coherently bounded on VO_2 nanorods on every faceted face with relatively moderate misfit energy. The uniaxial compressive lattice strain along the c_R axis induced by the misfit changed the relative thermodynamic stability of the low temperature M1 phase and the high temperature R phase while reducing the activation energy barrier for the phase transition. The remarkably reduced hysteresis loop width can ensure rapid response for applications in smart windows or other VO_2-based optoelectronic memory devices.

■ ASSOCIATED CONTENT

Ⓢ Supporting Information

Detailed calculation on the misfit and the synthesis, TEM images for W-doped VO_2 powders. This material is available free of charge via the Internet at http://pubs.acs.org.

■ AUTHOR INFORMATION

Corresponding Author

*E-mail: p-jin@mail.sic.ac.cn.

Notes

The authors declare no competing financial interest.

■ ACKNOWLEDGMENTS

This study was financially supported by the National Natural Science Foundation of China (NSFC, Nos: 51032008, 51272273, 51102270, 51272271, 51172265), the National Key Basic Research Program (NKBRP, 2009CB939904), and the high-tech project of MOST (2012AA030305, 2012BAA10B03).

■ REFERENCES

(1) Müller, J.; Lupton, J. M.; Lagoudakis, P. G.; Schindler, F.; Koeppe, R.; Rogach, A. L.; Feldmann, J.; Talapin, D. V.; Weller, H. *Nano Lett.* **2005**, *5*, 2044.
(2) Armstrong, T. R.; Buchanan, R. C. *J. Am. Ceram. Soc.* **1990**, *73*, 1268.
(3) Zeng, H.; Sun, S.; Li, J.; Wang, Z. L.; Liu, J. P. *Appl. Phys. Lett.* **2004**, *85*, 792.
(4) Smith, A. M.; Nie, S. *Acc. Chem. Res.* **2010**, *43*, 190.
(5) Smith, A. M.; Mohs, A. M.; Nie, S. *Nat. Nanotechnol.* **2009**, *4*, 56.
(6) Mitsuishi, T. *Jpn. J. Appl. Phys.* **1967**, *6*, 1060.
(7) Jin, P.; Tanemura, S. *Jpn. J. Appl. Phys.* **1994**, *33*, 1478.
(8) Manning, T. D.; Parkin, I. P. *J. Mater. Chem.* **2004**, *14*, 2554.
(9) Manning, T. D.; Parkin, I. P.; Blackman, C.; Qureshi, U. *J. Mater. Chem.* **2005**, *15*, 4560.
(10) Zhang, Z.; Gao, Y.; Chen, Z.; Du, J.; Cao, C.; Kang, L.; Luo, H. *Langmuir* **2010**, *26*, 10738.
(11) Kang, L. T.; Gao, Y. F.; Zhang, Z. T.; Du, J.; Cao, C. X.; Chen, Z.; Luo, H. J. *J. Phys. Chem. C* **2010**, *114*, 1901.
(12) Zhang, Z. T.; Gao, Y. F.; Kang, L. T.; Du, J.; Luo, H. J. *J. Phys. Chem. C* **2010**, *114*, 22214.
(13) Gao, Y.; Wang, S.; Kang, L.; Chen, Z.; Du, J.; Liu, X.; Luo, H.; Kanehira, M. *Energy Environ. Sci.* **2012**, *5*, 8234.
(14) Gao, Y.; Wang, S.; Luo, H.; Dai, L.; Cao, C.; Liu, Y.; Chen, Z.; Kanehira, M. *Energy Environ. Sci.* **2012**, *5*, 6104.
(15) Semenov, A. L. *Phys. Solid State* **2011**, *53*, 386.
(16) Liu, M. K.; Hwang, H. Y.; Tao, H.; Strikwerda, A. C.; Fan, K. B.; Keiser, G. R.; Sternbach, A. J.; West, K. G.; Kittiwatanakul, S.; Lu, J. W.; Wolf, S. A.; Omenetto, F. G.; Zhang, X.; Nelson, K. A.; Averitt, R. D. *Nature* **2012**, *487*, 345.
(17) Hu, B.; Ding, Y.; Chen, W.; Kulkarni, D.; Shen, Y.; Tsukruk, V. V.; Wang, Z. L. *Adv. Mater.* **2010**, *22*, 5134.
(18) Hu, B.; Zhang, Y.; Chen, W.; Xu, C.; Wang, Z. L. *Adv. Mater.* **2011**, *23*, 3536.
(19) Cao, J.; Gu, Y.; Fan, W.; Chen, L. Q.; Ogletree, D. F.; Chen, K.; Tamura, N.; Kunz, M.; Barrett, C.; Seidel, J.; Wu, J. *Nano Lett.* **2010**, *10*, 2667.
(20) Muraoka, Y.; Ueda, Y.; Hiroi, Z. In *8th ISSP International Symposium on Correlated Electrons (ISSP-Kashiwa 2001)*, Tokyo, Japan, 2001; p 965.
(21) Kikuzuki, T.; Lippmaa, M. *Appl. Phys. Lett.* **2010**, *96*, http://dx.doi.org/10.1063/1.3380599.
(22) Rini, M.; Cavalleri, A.; Schoenlein, R. W.; Lopez, R.; Feldman, L. C.; Haglund, R. F.; Boatner, L. A.; Haynes, T. E. *Opt. Lett.* **2005**, *30*, 558.
(23) Yang, T.-H.; Aggarwal, R.; Gupta, A.; Zhou, H. H.; Narayan, R. J.; Narayan, J. *J. Appl. Phys.* **2010**, *107*, http://dx.doi.org/10.1063/1.3327241.
(24) Nagashima, K.; Yanagida, T.; Tanaka, H.; Kawai, T. *Phys. Rev. B* **2006**, *74*, 172106.
(25) Nagashima, K.; Yanagida, T.; Tanaka, H.; Kawai, T. *J. Appl. Phys.* **2007**, *101*, http://dx.doi.org/10.1063/1.2424321.
(26) Li, Y.; Ji, S.; Gao, Y.; Luo, H.; Kanehira, M. *Sci. Rep.* **2013**, *3*, DOI: 10.1038/srep01370.
(27) Demirörs, A. F.; van Blaaderen, A.; Imhof, A. *Langmuir* **2010**, *26*, 9297.
(28) Hörlin, T.; Niklewski, T.; Nygren, M. *J. Phys. Colloques 37* **1976**, C4-69−C4-73, DOI: 10.1051/jphyscol:1976411.
(29) Lauhon, L. J.; Gudiksen, M. S.; Wang, C. L.; Lieber, C. M. *Nature* **2002**, *420*, 57.
(30) Zhu, M.; Chikyow, T.; Ahmet, P.; Naruke, T.; Murakami, M.; Matsumoto, Y.; Koinuma, H. *Thin Solid Films* **2003**, *441*, 140.
(31) Riesz, F. *J. Vac. Sci. Technol., A* **1996**, *14*, 425.
(32) Bales, G. S.; Zangwill, A. *Phys. Rev. B* **1990**, *41*, 5500.
(33) Ding, X.-Z.; Qi, Z. Z.; He, Y. Z. *J. Mater. Sci. Lett.* **1995**, *14*, 21.
(34) Matthews, J. W.; Blakeslee, A. E. *J. Cryst. Growth* **1974**, *27*, 118.
(35) Chudnovskii, F. A.; Stefanovich, G. B. *J. Solid State Chem.* **1992**, *98*, 137.
(36) Hörlin, T.; Niklewski, T.; Nygren, M. *Acta Chem. Scand. A* **1976**, *30*, 619.
(37) Ladd, L. A.; Paul, W. *Solid State Commun.* **1969**, *7*, 425.
(38) Du, J.; Gao, Y. F.; Luo, H. J.; Kang, L. T.; Zhang, Z. T.; Chen, Z.; Cao, C. X. *Sol. Energy Mater. Sol. Cells* **2011**, *95*, 469.
(39) Schmidt, V.; McIntyre, P. C.; Gösele, U. *Phys. Rev. B* **2008**, *77*, 235302.

(40) Kucharczyk, D.; Niklewski, T. *J. Appl. Crystallogr.* **1979**, *12*, 370.
(41) Straumanis, M. E.; Ejima, T.; James, W. J. *Acta Crystallogr.* **1961**, *14*, 493.
(42) Nishikawa, M.; Nakajima, T.; Kumagai, T.; Okutani, T.; Tsuchiya, T. *Jpn. J. Appl. Phys.* **2011**, *50*, 01BE04.
(43) Takahashi, I.; Hibino, M.; Kudo, T. *Jpn. J. Appl. Phys.* **2001**, *40*, 1391.
(44) Fu, G.; Polity, A.; Volbers, N.; Meyer, B. K. *Thin Solid Films* **2006**, *515*, 2519.
(45) Kang, M.; Kim, S. W.; Ryu, J. W.; Noh, T. *AIP Adv.* **2012**, *2*, 1.
(46) Felde, B.; Niessner, W.; Schalch, D.; Scharmann, A.; Werling, M. *Thin Solid Films* **1997**, *305*, 61.
(47) Gao, Y.; Cao, C.; Dai, L.; Luo, H.; Kanehira, M.; Ding, Y.; Wang, Z. L. *Energy Environ. Sci.* **2012**, *5*, 8708.
(48) Lu, Z.; Li, C.; Yin, Y. *J. Mater. Chem.* **2011**, *21*, 7.